rf barrier compression with space charge

Oliver Boine-Frankenheim

GSI Helmholtzzentrum für Schwerionenforschung GmbH, Planckstraße 1, D-64291 Darmstadt, Germany

(Received 24 August 2009; published 26 March 2010)

Because of the long synchrotron period between the two barriers, bunch compression in a barrier bucket is usually relatively slow. The conservation of the phase space area requires that the compression is performed adiabatically, that is much slower than the synchrotron period. We will show that the presence of longitudinal space charge can considerably improve the efficiency of the barrier compression. An optimized scheme using a novel ''shock'' compression is presented. The corresponding analytic model relies on the exact solution for shock waves in a cold beam. Results obtained from this model are compared with Vlasov simulations.

DOI: 10.1103/PhysRevSTAB.13.034202 PACS numbers: 29.27.Bd, 29.20.−c, 52.35.Tc, 52.59.Sa

I. INTRODUCTION

Barrier buckets are routinely employed in storage rings for the accumulation of antiprotons [1,2]. In synchrotrons for high intensity ion beams, barrier buckets are presently not a routine technique. In part this is due to beam loading and other high intensity effects that are of concern. Low Q magnetic alloy (MA) rf cavities are often used to generate single barrier pulses in the form of sinus half waves [3]. By moving one of the pulses one can, for example, compress the stored beam and open an empty gap for the next injection. At low and medium beam energies space charge effects play an important role. In Ref. [4] it was shown that space charge has the positive effect of increasing the threshold for the microwave instability in barrier buckets. It is the aim of the present study to point out additional beneficial effects of space charge below transition energy. More precisely we will show that space charge can reduce beam-loading effects and that it can significantly improve the performance of the barrier compression. As an example case, we consider the proposed precompression of an intense U^{28+} bunch at 1 GeV/u using two rf barrier pulses in the projected SIS-100 synchrotron [5]. The precompression is the most demanding rf manipulation during the SIS-100 cycle. It prepares the bunch for the subsequent fast (0.1 ms) bunch rotation just before extraction. The total cycle time of SIS-100 is 1 s, roughly. The precompression should be completed in about $T = 100$ ms in order to meet the required average beam intensities on the production target. Alternative precompression schemes for SIS-100 based on batch compression and conventional rf buckets at different harmonics were studied in Ref. [6] for low beam intensities. In the barrier compression scheme, one starts from a long bunch of length $l_0 \approx 0.8L$ (SIS-100 ring circumference $L = 2\pi R = 1080$ m) confined between two rf barrier half waves. One of the barriers is moved inside the bunch for precompression up to $l_1 \approx 0.4L$. Because of the expected low momentum spread of initially $(\Delta p/p)_{\mathrm{rms}} \approx 10^{-4}$ and the corresponding small synchrotron period of $T_s \approx 300$ ms, the compression cannot be truly adiabatic. However, for low momentum spreads and high beam intensities ($N = 5 \times 10^{11}$ U^{28+} ions), space charge effects play an important role in SIS-100. A novel ''shock'' compression scheme for space charge dominated beams will be described and applied to the conditions in SIS-100. Although the present study focuses on parameters that are of relevance for the SIS-100 project, the presented compression scheme and especially the shock wave solutions for space charge dominated beams are also of more general interest. The structure of this paper is as follows: In Sec. II the distortion of the rf barrier potential due to space charge is analyzed. In Sec. III the combined effect of beam loading and space charge in a stationary bunch is treated. Section IV deals with the nonadiabatic barrier compression of a low intensity bunch. In Sec. V the shock compression is presented and compared to Vlasov simulation. Barrier compression schemes with space charge are presented in Sec. VI. The conclusions are in Sec. VII.

II. POTENTIAL DISTORTION DUE TO SPACE CHARGE

The stationary line density profile for a bunch that is confined between two barrier rf half waves is obtained assuming a local elliptic distribution [7]. The local elliptic distribution has the main advantage that the local space charge voltage is directly proportional to the local rf voltage. For strong space charge the bunch profiles obtained from an elliptic and from a Gaussian distribution agree (see e.g. [8], page 412). Let z and v be the deviations in position and velocity from the particle at rest in the bucket center, then the longitudinal equation of motion is

$$\dot{v} = \frac{1}{m^*}\frac{qV}{L}, \qquad \dot{z} = v \tag{1}$$

with the effective mass $m^* = -\gamma_0 m/\eta_0$, the relativistic parameter γ_0, the slip factor $\eta_0 = 1/\gamma_t^2 - 1/\gamma_0^2$, the transition parameter γ_t, the ring circumference L, the charge q, the mass m, and the voltage profile $V(z)$. The equation of

motion in the (z, v) coordinates can be derived from the "Hamiltonian"

$$H = \frac{v^2}{2} - \frac{qV_0}{m^* L} Y(z). \tag{2}$$

The potential function is

$$Y(z) = \frac{1}{V_0} \int_0^z V dz, \tag{3}$$

where V_0 is the rf voltage amplitude. The line density resulting from an elliptic bunch distribution is [7,9]

$$\lambda(z) = \lambda_0 \left(1 - \frac{Y(z)}{Y(z_m)}\right). \tag{4}$$

λ_0 is the line density in the bunch center. The potential function at the bunch ends $z = z_m$ can be obtained from Eq. (2) as

$$Y(z_m) = -\frac{Lm^* v_m^2}{2qV_0}, \tag{5}$$

where $v_m = -\eta_0 \beta_0 c \Delta p/p$ is the maximum velocity of the particle at the bunch boundary and $\Delta p/p$ the maximum momentum spread in the bunch.

The voltage profile $V(z)$ can be divided into the external (rf) voltage part and the space charge part. The rf voltage profile for a conventional rf bucket is $V_{\rm rf}(z) = V_0 \sin(hz/R)$, where h is the harmonic number of the rf wave. In a barrier bucket the right part of the half wave is shifted towards positive z and the left part towards negative z (see the black curve in Fig. 1). Below transition the total focusing voltage applied to the beam is then $V = -V_{\rm rf} + V_{\rm sc}$, where the space charge voltage is defocusing. Here we will focus on the case below transition, above transition $V = V_{\rm rf} + V_{\rm sc}$ would apply. The space charge voltage is given through [9,10]

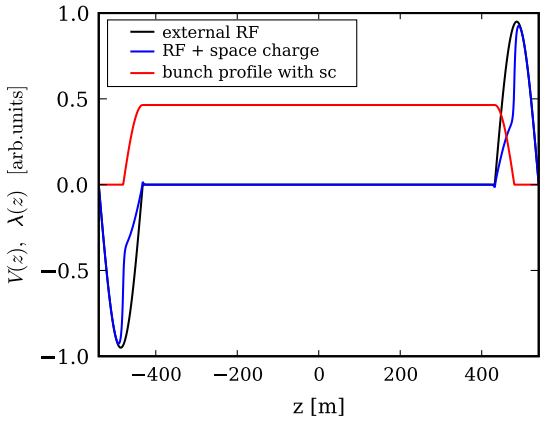

FIG. 1. (Color) Matched bunch and voltage profiles between two barrier rf half waves (harmonic number $h = 5$) for $\Sigma = 2$. Shown are the bunch profile (red curve), the external rf voltage (black curve), and the total voltage (blue curve).

$$V_{\rm sc}(z) = -q\beta_0 c X_{\rm sc} R \frac{\partial \lambda}{\partial z} \tag{6}$$

and the corresponding space charge potential is

$$Y_{\rm sc}(z) = q\beta_0 c \frac{RX_s}{V_0} (\lambda_0 - \lambda), \tag{7}$$

where $X_{\rm sc}$ is the space charge reactance

$$X_{\rm sc} = \frac{g}{2\epsilon_0 \beta_0 c \gamma_0^2} \tag{8}$$

and $g = 0.5 + 2\ln(b/a)$ is the g factor. The space charge factor defined as

$$\Sigma = \frac{1}{\frac{V_{\rm rf}}{V_{\rm sc}} - 1} \tag{9}$$

describes the space charge induced voltage reduction inside a matched bunch. For an elliptic bunch distribution, the local space charge voltage is directly proportional to the local rf voltage and Σ, as defined above, is constant. From Eqs. (4) and (6) the space charge factor can be derived as

$$\Sigma = 2\frac{c_{s0}^2}{v_m^2} \tag{10}$$

with

$$c_{s0} = \sqrt{\frac{qX_{\rm sc} I_0}{2\pi m^*}}, \tag{11}$$

where I_0 is the current in the bunch center. Equation (10) applies also to the region between rf barriers. In this case I_0 is the current between the barriers and the space charge factor Σ can be interpreted in terms of the ratio of the coherent phase velocity c_{s0} of space charge waves and the incoherent velocity v_m [4]. Between two rf barriers the force is zero ($Y = 0$) and the line density is constant $\lambda(z) = \lambda_0$, if we only account for space charge effects. Equation (6) implies a constant space charge impedance $Z_{\rm sc} = -inX_{\rm sc}$, with the harmonic number n. Close to the cutoff frequency of the beam pipe (at harmonic n_c) the space charge impedance drops according to [11]

$$Z_{\rm sc} = -\frac{inX_{\rm sc}}{1 + (n/n_c)^2} \approx -inX_{\rm sc}\left(1 - \frac{n^2}{n_c^2}\right) \tag{12}$$

and the resulting first correction term to the space charge voltage in Eq. (6) is (see also Ref. [12])

$$\Delta V_{\rm sc}(z) = q\beta_0 c X_{\rm sc} \frac{R^3}{n_c^2} \frac{\partial^3 \lambda}{\partial z^3}. \tag{13}$$

As we will see later in Sec. V, this correction term causes dispersion effects in the equation of motion. However, for the calculation of the potential deformation we will assume a constant space charge impedance, which is a valid approximation if the shoulders of the bunch are long com-

pared to the cutoff wavelength L/n_c. The matched bunch profile for parameters relevant at the SIS-100 extraction energy (see Table I) is shown in Fig. 1. The deformation of the total voltage profile is clearly visible.

III. BEAM-LOADING EFFECTS

Beam loading in the rf cavities is a major reason for the asymmetric bunch form distortion at high beam intensities (see, e.g., Refs. [13,14]). Especially in barrier buckets beam loading can have a dramatic effect on the bunch form, because of the missing rf force between the barriers. Here we assume a broadband MA cavity with a constant impedance $Z^{\mathrm{bl}} \approx R_s$ (shunt impedance R_s). This approximation applies to the MA cavities that are projected for the barrier bucket generation in SIS-100. The corresponding beam-loading potential is

$$Y_{\mathrm{bl}}(z) = -q\beta_0 c \frac{R_s}{V_0} \int_0^z \lambda dz. \tag{14}$$

Between the barriers $Y_{\mathrm{rf}} = 0$ holds and from Eq. (4) one obtains the following differential equation for the line density:

$$\lambda' = -\Sigma\lambda' - \lambda_0 \alpha_r \lambda, \tag{15}$$

where Σ is the space charge parameter and α_r is the beam-loading coefficient

$$\alpha_r = \frac{2q^2\beta_0 c R_s}{Lm^* v_m^2}. \tag{16}$$

The resulting expression for the line density between the barriers is

$$\lambda(z) = \lambda_0 \exp\left(-\frac{\lambda_0 \alpha_r}{1+\Sigma} z\right). \tag{17}$$

For small arguments we obtain for the line density perturbation $\Delta\lambda = \lambda - \lambda_0$,

$$\frac{\Delta\lambda(z)}{\lambda_0} \approx -\frac{\lambda_0 \alpha_r}{1+\Sigma} z. \tag{18}$$

If we equate z with the half-bunch length z_m, we can define a beam-loading parameter including space charge

$$\Sigma_r = \frac{\lambda_0 \alpha_r z_m}{1+\Sigma}. \tag{19}$$

For $\Sigma_r \lesssim 1$ beam-loading effects can be assumed to be weak. This criterium also defines the tolerable R_s for the SIS-100 barrier rf cavities. In Fig. 2 we plot the bunch forms and the voltage functions with space charge and beam loading (blue curves) and for beam loading without space charge (red curves). The results were obtained via numerical iteration of Eq. (4). By adjusting the shunt impedance R_s the beam-loading parameter in Fig. 2 is chosen as $\Sigma_r = 2$ for the space charge parameter $\Sigma = 2$. The beam parameters are the same as those used for Fig. 1.

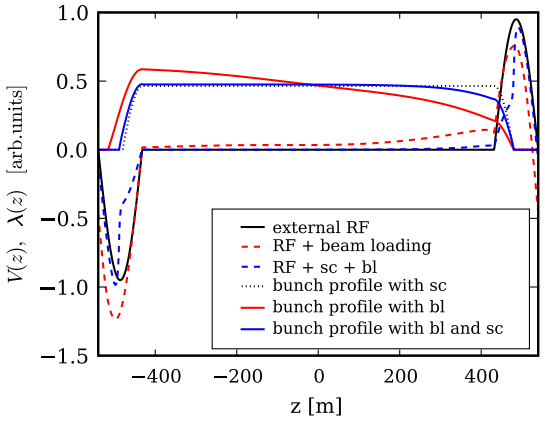

FIG. 2. (Color) Matched bunch and voltage profiles between two barrier rf half waves for $\Sigma = 2$ and $\Sigma_r = 2$ (blue curves). The red curves represent the results for $\Sigma = 0$ and $\Sigma_r = 2$.

We see that space charge acts as a kind of passive feedback mechanism that tends to restore a symmetric bunch profile. It is important to note that Eq. (19) is valid also for a Gaussian bunch distribution. In the following sections we will always assume that beam-loading effects can be ignored $\Sigma_r \ll 1$.

IV. NONADIABATIC BARRIER COMPRESSION

In order to compress the bunch, the phase of one barrier rf wave is varied (see e.g. [1]) and the barrier moves with the velocity $u_b = \dot{l}$ into the beam. l is the distance between the barriers. Adiabatic barrier compression requires that the barrier velocity is much slower than the incoherent velocity $u_b \ll v_m$ [1]. An adiabatic compression ramp can be derived from

$$\frac{1}{l}\frac{dl}{dt} = -\frac{\mu}{T_s(l)}, \tag{20}$$

where μ, as defined in the above equation, is the adiabaticity parameter and $T_s \approx 2l/v_m$ is the synchrotron period for particles at the bunch boundary. Adiabatic compression requires $\mu \ll 1$. If T_{s0} is the synchrotron period of a boundary particle before compression, then the synchrotron period during compression is $T_s(l) = T_{s0} l^2/l_0^2$, where l_0 is the initial barrier distance. During adiabatic compression the bunch area $A_b \approx 2v_m l$ remains constant and therefore T_s decreases with l^2/l_0^2 because the velocity of a particle at the bunch boundary increases according to $v_m \sim l_0/l$. With these definitions, Eq. (20) yields

$$l = l_0\sqrt{1 - 2\mu\frac{t}{T_{s0}}}. \tag{21}$$

As an example, for a final barrier distance $l_1 = l_0/2$ the corresponding compression time is $T/T_{s0} = 3/(8\mu)$. If we chose a ramp time $T = T_{s0}$ the resulting adiabaticity parameter is $\mu = 3/8$. In SIS-100 the compression should be

completed within $T \approx 100$ ms, but the initial synchrotron period is already $T_{s0} = 300$ ms. Therefore an adiabatic compression is not possible and we deliberately attempt an optimized nonadiabatic compression scheme with a constant barrier velocity $u_b \lesssim v_m$. Let us first neglect space charge effects by assuming $\Sigma = 0$. The maximum velocity v_m changes at the moving barrier to $v_{m1} = -(v_m + 2u_b)$. In the proposed scheme the compression stops exactly at the time the particle with initial velocity $-(v_m + 2u_b)$ and initial position at the barrier z_m is reflected at the stationary barrier and reaches the moving barrier again. In this way no particle hits the moving barrier more than once. The compression time for this scheme is

$$T = \frac{\Delta l}{u_b} = \frac{l_0 + l_1}{v_m + 2u_b}, \tag{22}$$

where $\Delta l = l_0 - l_1$ is the compression length. From the above equation we obtain

$$u_b = v_m\left(\frac{2l_0}{\Delta l} - 3\right)^{-1}, \tag{23}$$

which yields $u_b/v_m = 1$ and $T \approx 70$ ms for $\Delta l = l_0/2$ and SIS-100 parameters (see Table I). The scheme can be applied in SIS-100 because the precompressed bunch will be rotated and extracted in less than a millisecond. Figure 3 shows the final beam distribution obtained from a Vlasov simulation [4]. The increase of the bunch area due to the emerging voids in the occupied phase space area is clearly visible. During compression the rms bunch area increases by roughly the factor 1.5, which is in agreement with the analytic estimate

$$\frac{A_{b1}}{A_{b0}} = \left(1 - \frac{\Delta l}{l_0}\right)\left(1 + 2\frac{u_b}{v_m}\right), \tag{24}$$

where $A_{b0} \approx 2v_m l_0$ is the initial bunch area and $A_{b1} \approx 2(v_m + 2u_b)l_1$ is the final bunch area. It is important to note that alternative fast barrier compression schemes exist (see, e.g., Ref. [15]).

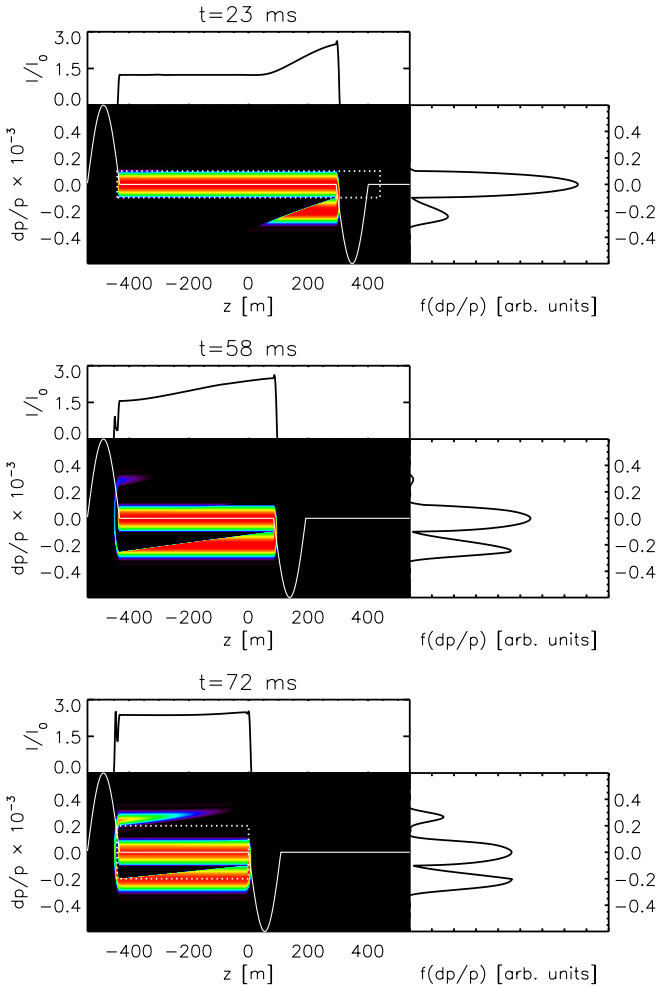

FIG. 3. (Color) Snapshots of the bunch distribution during barrier compression obtained from the simulation. The barrier velocity is $u_b = v_m$ and space charge effects are neglected. The dotted rectangles indicate the initial bunch boundary (top) and the final one (bottom), assuming that the bunch area is conserved $A_{b0} = A_{b1}$.

V. SHOCK COMPRESSION

In this section we will study the barrier compression of beams affected by space charge. First we will obtain an analytic solution for shock waves in space charge dominated beams. In the limit of a space charge dominated beam with $c_{s0} \gg v_m$, the Vlasov equation for the evolution of the distribution function can be reduced to the cold fluid equations for the line density $\lambda(z)$ and the local velocity $u(z)$ (see Refs. [8,16]):

$$\frac{\partial \lambda}{\partial t} + \frac{\partial}{\partial z}(\lambda u) = 0 \qquad \frac{\partial u}{\partial t} + u\frac{\partial u}{\partial z} + \chi\frac{\partial \lambda}{\partial z} = 0 \tag{25}$$

with

$$\chi = \frac{qX_{\mathrm{sc}}\beta_0 c}{2\pi m^*}. \tag{26}$$

The cold fluid equations can be obtained directly from the equation of motion $du/dt = qV/(Lm^*)$ and Eq. (6) for the space charge voltage $V = V_{\mathrm{sc}}$. The cold fluid equations comply with Euler's fluid equations for the equation of state $p = \chi\lambda^\gamma/2$ with $\gamma = 2$. It is well known that for a piston moving into a gas Euler's fluid equations exhibit a shock wave solution [17]. In our compression scheme the barrier moving with the constant velocity u_b acts like a piston. The resulting shock velocity is c_s. In Fig. 4 the shock front propagation is depicted. λ_1 is the line density in front of the moving barrier. λ_0 is the unperturbed line density. The cold fluid equations (25) can be rewritten in the following form reflecting the conservation of the particle number and momentum:

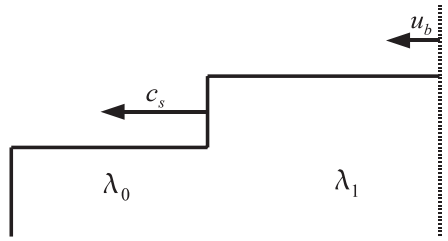

FIG. 4. Shock front moving with the velocity c_s from the barrier (velocity u_b) into the undisturbed beam.

$$\frac{\partial \lambda}{\partial t} = -\frac{\partial}{\partial z}(\lambda u) \qquad \frac{\partial(\lambda u)}{\partial t} = -\frac{\partial}{\partial z}\left(\frac{\chi}{2}\lambda^2 + \lambda u^2\right). \tag{27}$$

The integration of the above equations across the shock front, assuming an infinitely thin shock layer, yields

$$\lambda_0 u_0 = \lambda_1 u_1 \qquad \frac{\chi}{2}\lambda_0^2 + \lambda_0 u_0^2 = \frac{\chi}{2}\lambda_1^2 + \lambda_1 u_1^2, \tag{28}$$

where $u_0 = c_s$ and $u_1 = c_s - u_b$ are the velocities in the unperturbed beam and in the compressed beam relatively to the shock layer. Eliminating the compressed density λ_1 in Eqs. (28) leads to

$$2c_s(c_s - u_b)^2 = c_{s0}^2(2c_s - u_b). \tag{29}$$

For weak shocks with $u_b \ll c_{s0}$ we obtain $c_s \approx c_{s0}$. For larger ratios we can use the exact expression

$$c_s' = 2\sqrt{-Q}\cos\left(\frac{\theta}{3}\right) + \frac{2}{3}u_b', \tag{30}$$

where $c_s' = c_s/c_{s0}$ is the normalized shock velocity and $u_b' = u_b/c_{s0}$ is the normalized barrier velocity or Mach number. The other quantities are

$$\theta = \arccos\left(\frac{R}{\sqrt{-Q^3}}\right)$$

and

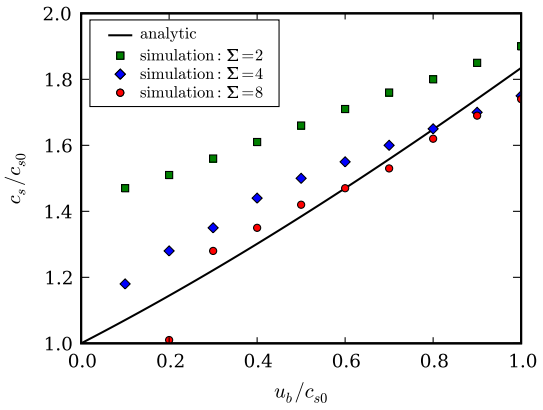

FIG. 5. (Color) Shock velocity c_s as a function of the barrier velocity u_b obtained from Eq. (30) and from simulations for three different space charge parameters.

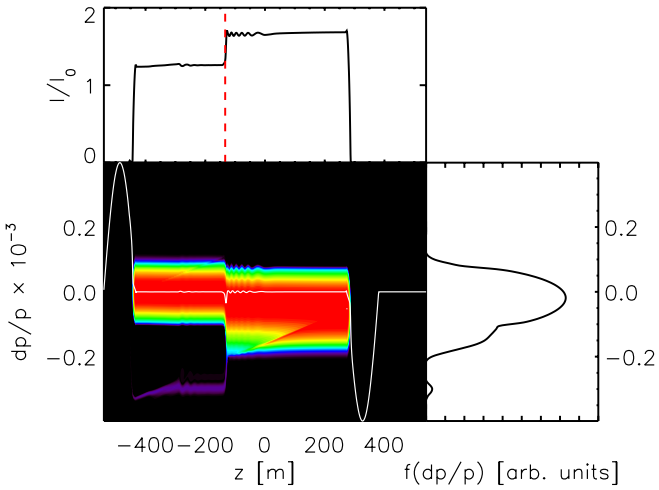

FIG. 6. (Color) Snapshot of the shock front for $\Sigma = 4$ and $u_b = 0.4c_{s0}$ from the simulation.

$$R = -\frac{1}{27}u_b'^3 + \frac{1}{12}u_b', \qquad Q = -\frac{1}{9}u_b'^2 - \frac{1}{3}.$$

The resulting curve for $c_s'(u_b')$ is shown in Fig. 5. The curve can be well approximated by a linear dependence $c_s' = 1 + \alpha u_b'$ with $\alpha \approx 0.8$. The symbols represent results obtained from a self-consistent Vlasov simulation code [4] for different space charge parameters. In the simulation we moved the right barrier with a constant velocity u_b into the bunch. The velocity of the resulting shock front c_s was obtained from the simulation. One can observe in Fig. 5 that the agreement between the simulation results and Eq. (30) improves with increasing Σ. For moderate space charge ($\Sigma = 2$) the shock velocity c_s obtained from the simulation is underestimated by Eq. (30). For large Σ and low barrier Mach numbers u_b' the shock front decays into localized coherent structures. The shock solutions obtained from the simulations will be analyzed in the following. Figures 6–9 show the shock fronts for different Σ and u_b' indicated by the vertical red dashed lines. The shock front for $\Sigma = 4$ and $u_b' = 0.4$ is shown in Fig. 6. In front of the shock wave (moving to the left), we observe a filament of particles that are reflected from the space charge field of the shock front. In a cold beam the particle velocity drops from u_0 to u_1 (in the frame moving with the shock front) when a particle penetrates the shock front. In a "warm" beam with a finite momentum spread the kinetic energy of particles at the lower edge of the velocity distribution at $u_0 - v_m$ can be too low to penetrate the shock front; instead they are reflected. The density of reflected particles can be expected to increase with the barrier velocity (see Fig. 7), because the relative height of the shock front λ_1/λ_0 increases with u_b. With increasing Σ the shock front velocity increases and for $c_{s0} \gg v_m$ the beam again behaves like a cold beam. The reflected particles are potentially lost from the rf bucket provided by the barriers. The reflected particles are a possible reason for the discrepancy

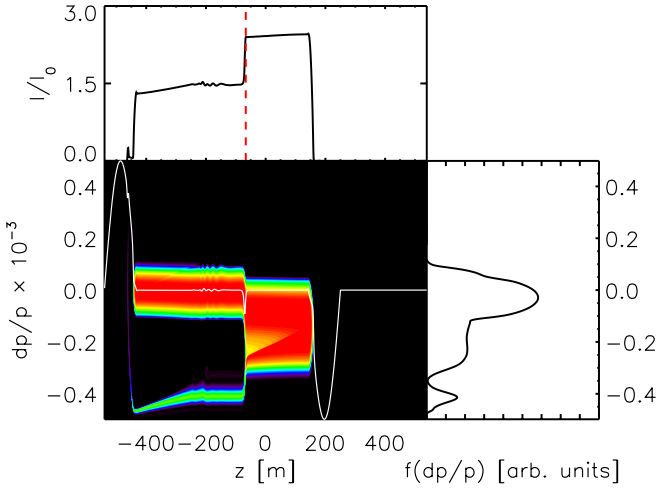

FIG. 7. (Color) Snapshot of the shock front for $\Sigma = 4$ and $u_b = c_{s0}$ from the simulation.

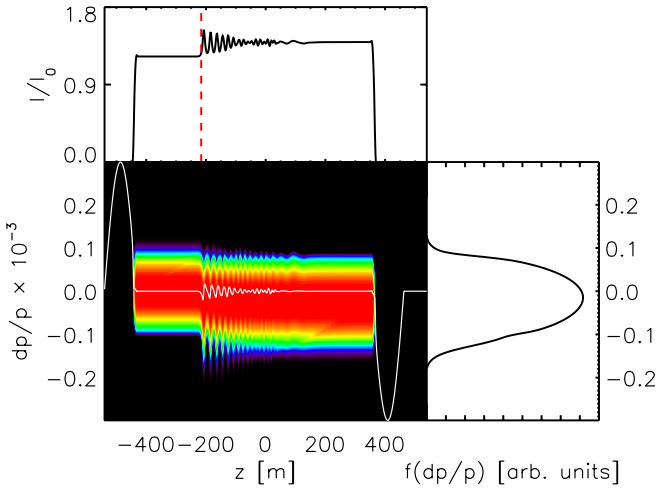

FIG. 8. (Color) Snapshot of the shock front for $\Sigma = 8$ and $u_b = 0.2c_{s0}$ from the simulation.

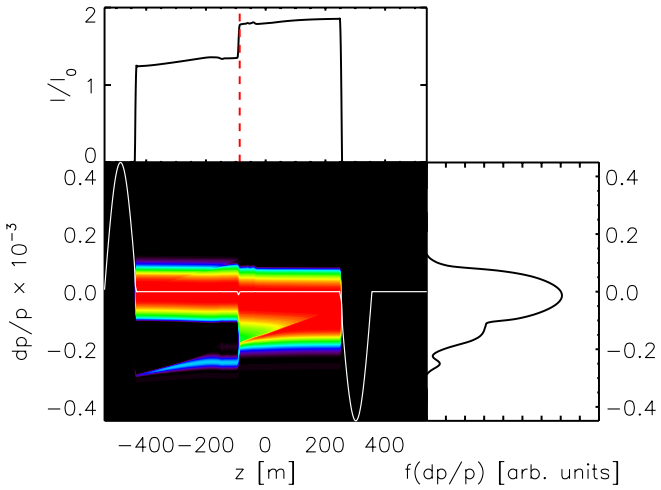

FIG. 9. (Color) Snapshot of the shock front for $\Sigma = 2$ and $u_b = 0.6c_{s0}$ from the simulation.

between the analytic result and the simulation result in Fig. 5 for larger u_b'. For low barrier velocities ($u_b' \lesssim 0.2$) and large Σ, the shock front decays into localized coherent structures (see Fig. 8). This is due to the dispersion induced by the drop-off of the space charge impedance [12,18]. In Fig. 9 the simulation result for $\Sigma = 2$ and $u_b' = 0.5$ is shown. For lower Σ the line density behind the shock front (to the right) starts to develop a slope, similar to the result for $\Sigma = 0$ (see Fig. 3).

In summary we find from our Vlasov simulations that, for space charge parameters $\Sigma \gtrsim 1$ and $\Sigma \lesssim 10$, shock solutions exist that can be used for barrier compression, provided that the relative number of reflected particles remains tolerable. For $\Sigma \gtrsim 3$ the shock velocities c_s obtained from the simulations agree rather well with the analytic result for a cold beam Eq. (30).

VI. BARRIER COMPRESSION SCHEMES WITH SPACE CHARGE

After the analytical and numerical analysis of shock waves in space charge dominated beams we turn again to the barrier compression schemes. We focus on the parameters and requirements for the bunch precompression in SIS-100 that are summarized in Table I. The most simple approach would be to move one barrier with constant velocity u_b until the shock front reaches the opposite barrier. The compression time for this scheme is

$$T = \frac{\Delta l}{u_b} = \frac{l_0}{c_s}. \tag{31}$$

The resulting barrier Mach number for a given compression factor $\Delta l/l_0$ is

$$u_b' = \left(\frac{l_0}{\Delta l} - \alpha\right)^{-1}, \tag{32}$$

where we used the approximate expression $c_s' = 1 + \alpha u_b'$ found in the previous section. For the compression factor $\Delta l/l_0 = 0.5$ required in the SIS-100, the barrier Mach number is $u_b' \approx 0.83$. For $\Sigma = 2$ one has to use the exact numerical values for c_s' (see Fig. 5) instead of the analytic result. Still the obtained barrier Mach number of $u_b' \approx 0.86$ is very similar. For these Mach numbers the relative number of particles reflected from the shock front is already high (see Sec. V). In addition the final compressed bunch has an undesired velocity offset of $-u_b$ (see, e.g., Fig. 7). Therefore we use a compression scheme similar to the one presented in Sec. IV. In this scheme the compression time is tuned exactly in such a way that the shock front returns back to the moving barrier after being reflected at the fixed barrier. The resulting compression time is

$$T = \Delta l/u_b \approx (l_0 + l_1)/c_s, \tag{33}$$

where the last relation is only approximative because the reflected shock front moves through an increased bunch density. The resulting barrier Mach number is

TABLE I. SIS-100 parameter.

L [m]	γ_t	V_0 [kV]	h	Ion	N	γ_0	$(\Delta p/p)_0$	Σ_0	c_{s0} [km/s]	l_0	l_1
1080	15.6	16	5	U^{28+}	5×10^{11}	2.1	10^{-4}	2	6	$0.8L$	$0.4L$

$$u_b' \approx \left(\frac{2l_0}{\Delta l} - 1 - \alpha\right)^{-1}, \tag{34}$$

which gives $u_b' \approx 0.45$ for $\Delta l/l_0 = 0.5$. For $\Sigma = 4$ the resulting compressing time is $T \approx 110$ ms. For larger Σ the compression time T can be shorter relative to the $\Sigma = 0$ case, because the relevant velocity in Eq. (34) is c_{s0} and not v_m, like in Eq. (23). However, the more important aspect is that during the shock compression the growth of the bunch area is very small, provided that the barrier Mach number remains below $\lesssim 0.6$. This will be demonstrated using Vlasov simulations. Figure 10 shows snapshots of the barrier compression using the parameters given in Table I. The steep shock front launched from the moving barrier is clearly visible (top). In about $T = 140$ ms, the shock front returns back to the moving barrier and the compression is completed (bottom). In this simulation the slightly higher barrier Mach number of $u_b' = 0.56$ was used, which results from Eq. (31) if one uses the numerically obtained exact c_s' for $\Sigma = 2$ from Fig. 5. Using this exact c_s', Eq. (31) predicts a slightly shorter compression time of $T = 135$ ms. In Fig. 10 one can observe that the phase space area occupied by the bunch is very well conserved during the shock compression. The

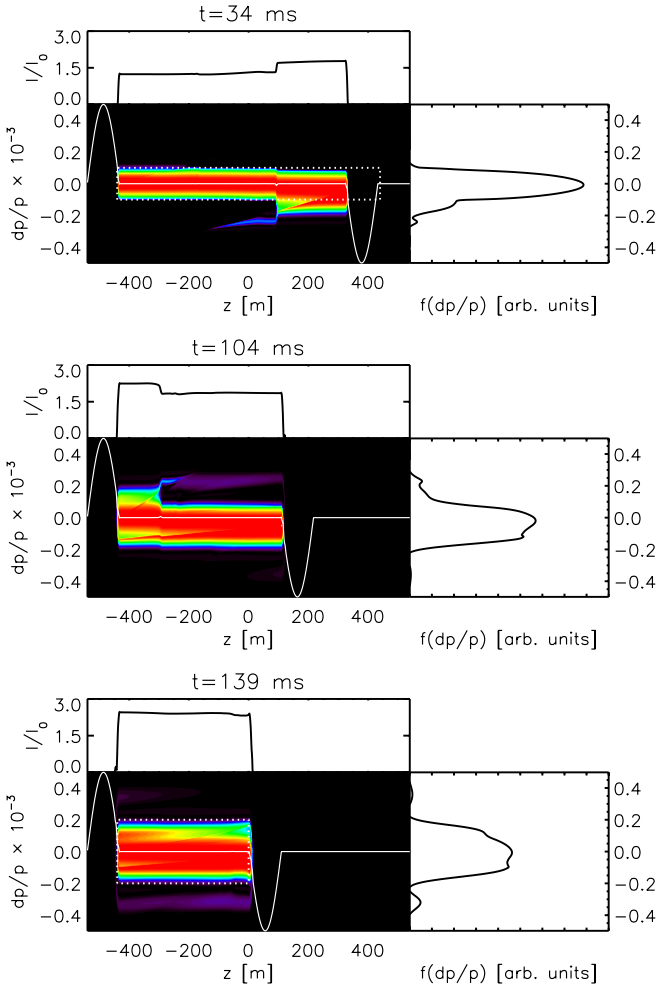

FIG. 10. (Color) Snapshots of the beam distribution during barrier compression obtained from a Vlasov simulation for $\Sigma = 2$ and $u_b = 0.56c_{s0}$. The dotted rectangles indicate the initial bunch boundary (top) and the final one (bottom), assuming that the bunch area is conserved $A_{b0} = A_{b1}$.

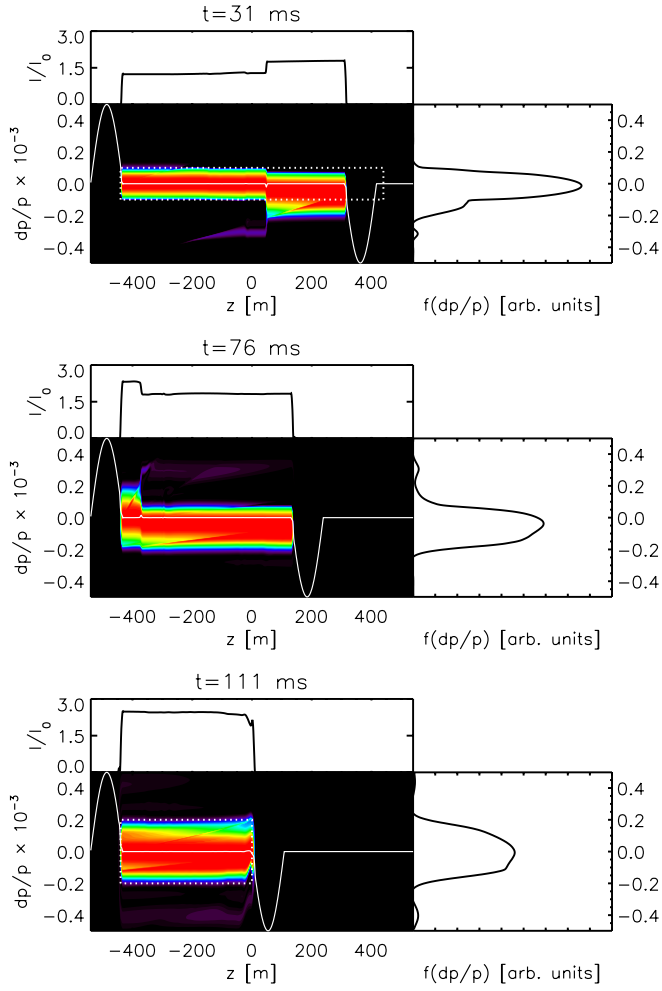

FIG. 11. (Color) Snapshots of the beam distribution during barrier compression obtained from a Vlasov simulation for $\Sigma = 4$ and $u_b = 0.45c_{s0}$. The dotted rectangles indicate the initial bunch boundary (top) and the final one (bottom), assuming that the bunch area is conserved $A_{b0} = A_{b1}$.

particles reflected from the shock front are in a filament outside the dotted rectangle in Fig. 10 (bottom). This filament represents less than 5% of the total bunch intensity. Figure 11 shows snapshots of the barrier compression for the larger space charge parameter $\Sigma = 4$. The barrier Mach number is $u_b' = 0.45$. As also predicted by Eqs. (33) and (34) in about $T = 110$ ms the compression is completed. The particles outside the dotted rectangle in Fig. 11 (bottom) are in a filament that represents less than 2% of the total bunch intensity. The shock compression for the even larger space charge parameter $\Sigma = 8$ is shown in Fig. 12. Again the compression time of $T = 85$ ms agrees quite well with the analytic estimate from Eqs. (33) and (34) ($T = 81$ ms). For this large space charge parameter the reflected particles outside the dotted rectangle in Fig. 12 (bottom) represent only less than 1% of the total bunch intensity.

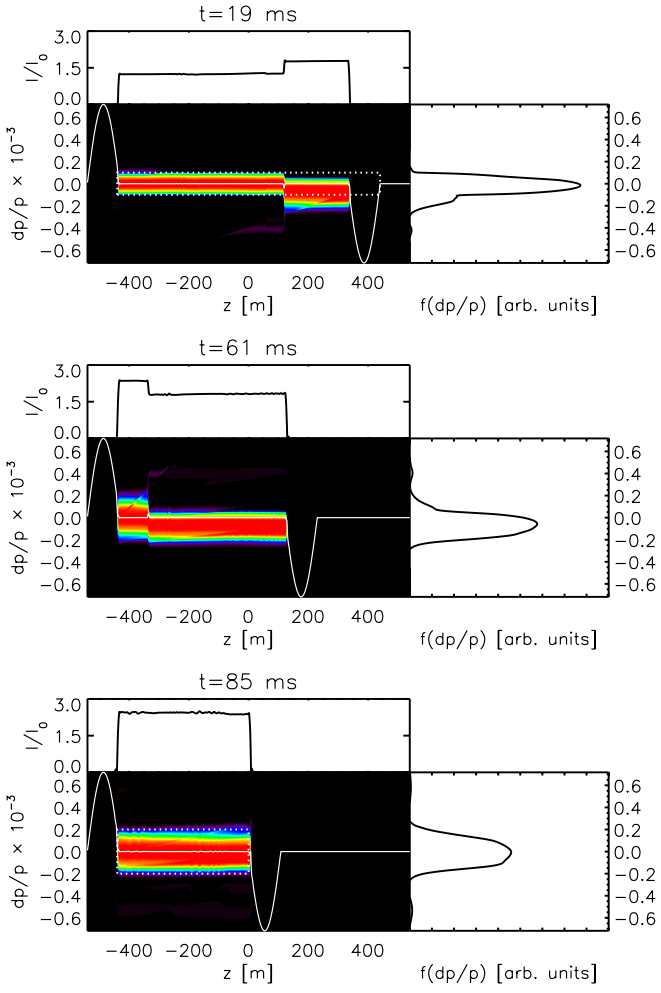

FIG. 12. (Color) Snapshots of the beam distribution during barrier compression obtained from a Vlasov simulation for $\Sigma = 8$ and $u_b = 0.45 c_{s0}$. The dotted rectangles indicate the initial bunch boundary (top) and the final one (bottom), assuming that the bunch area is conserved $A_{b0} = A_{b1}$.

VII. CONCLUSIONS

In this study we showed that longitudinal space charge can act in beneficial ways. First, space charge can reduce the asymmetric bunch deformation induced by beam loading. This is particularly important in long barrier buckets. Second, space charge can improve the efficiency of rf manipulations. A barrier compression scheme for space charge dominated bunches is presented. The scheme takes advantage of the shock front that launches naturally if a barrier moves into a space charge dominated beam. The duration of the compression depends on the velocity of the shock front c_s and not on the incoherent velocity spread v_m. Vlasov simulation showed that for space charge dominated beams the shock velocity c_s is in good agreement with the analytic result obtained for a cold beam. During the shock compression the bunch area is conserved very well. For barrier Mach numbers approaching $u_b' = 1$, the bunch area increases due to particles that are reflected at the shock front. For large space charge parameters dispersion effects can lead to a decay of the shock front into localized coherent structures. Using the expected beam parameters in SIS-100, the simulations demonstrate that the scheme can potentially be employed for the precompression step. Shocks generated by moving barriers might have other applications, e.g., in low-energy, cooled ion beams. As a next step, we would like to repeat experiments [19] performed at GSI with a moving barrier, but with high current ion beams in order to observe the shock wave.

ACKNOWLEDGMENTS

The author would like to thank Heiko Damerau, CERN, for his important comments. Also the author wishes to express his gratitude to the anonymous referee who considerably helped to improve this work.

[1] S. Y. Lee and K. Y. Ng, Phys. Rev. E **55**, 5992 (1997).
[2] C. M. Bhat, in *Proceedings of the 9th European Particle Accelerator Conference, Lucerne, 2004* (EPS-AG, Lucerne, 2004), p. 236.
[3] M. Fujieda *et al.*, Phys. Rev. ST Accel. Beams **2**, 122001 (1999).
[4] O. Boine-Frankenheim and I. Hofmann, Phys. Rev. ST Accel. Beams **6**, 034207 (2003).
[5] FAIR baseline technical report, Vol. 2 (2006).
[6] H. Damerau, CERN-Thesis-2005-048, 2005, p. 159.
[7] A. Hofmann and F. Pedersen, IEEE Trans. Nucl. Sci. **26**, 3526 (1979).
[8] M. Reiser, *Theory and Design of Charged Particle Beams* (Wiley-VCH, New York, 2004).
[9] O. Boine-Frankenheim and T. Shukla, Phys. Rev. ST Accel. Beams **8**, 034201 (2005).
[10] D. Neuffer, Part. Accel. **11**, 23 (1980).
[11] A. Al-Khateeb, O. Boine-Frankenheim, I. Hofmann, and G. Rumolo, Phys. Rev. E **63**, 026503 (2001).

[12] R. Davidson, Phys. Rev. ST Accel. Beams **7**, 054402 (2004).
[13] K. Y. Ng, *Physics of Intensity Dependent Beam Instabilities* (World Scientific, Singapore, 2006), p. 75.
[14] C. M. Bhat and K. Y. Ng, Report No. FERMILAB-Conf-03/395-T, 2004.
[15] G. W. Foster, C. M. Bhat, B. Chase, K. Seiya, J. A. MacLachlan, P. Varghese, and D. Wildman, Proceedings of the 9th European Particle Accelerator Conference, Lucerne, 2004 (Ref. [2]), 1479.
[16] G. Rumolo *et al.*, Phys. Plasmas **6**, 4349 (1999).
[17] Ya. B. Zel'dovich and Yu. P. Raizer, *Physics of Shock Waves and High-Temperature Hydrodynamic Phenomena* (Dover, New York, 2002), p. 45.
[18] O. Boine-Frankenheim and I. Hofmann, Phys. Rev. ST Accel. Beams **3**, 104202 (2000).
[19] C. Dimopoulou, B. Franzke, T. Katayama, F. Nolden, G. Schreiber, and M. Steck, Proc. COOL **07**, 21 (2007).